



# Electromechanical Dynamic Analysis of the Integrated System of Switched Reluctance Motor and Planetary Gear Transmission

Ruibo Chen<sup>1</sup> · Changzhao Liu<sup>1</sup> · Datong Qin<sup>1</sup> · Xiaoqi Dong<sup>1</sup>

Received: 6 July 2021 / Revised: 17 September 2021 / Accepted: 25 September 2021 / Published online: 12 October 2021  
© Krishtel eMaging Solutions Private Limited 2021

## Abstract

**Background and Purpose** Switched reluctance motors (SRMs) are a good choice for electric vehicle motors, because the rare-earth elements are not necessary. Planetary gear transmission (PGT) has a large transmission ratio, high power density, and compact structure. Therefore, the integrated electric driving system of the SRM-PGT is the development direction for electric vehicle power transmission. The integrated electric driving system of the SRM-PGT is proposed in this paper.

**Methods** Aiming at this system, the dynamic model of the mechanical system is constructed using the reduced-order finite-element method, which considers the flexibility of the gearbox, stator, ring gear, and carrier. A dynamic model of the SRM is simultaneously constructed to obtain the nonlinear spatio-temporal electromagnetic torque and radial force waves. Finally, a coupling dynamic model, including the mechanical, electric, and control systems, is built. The interaction between the PGT and SRM with and without coupling is investigated under steady-state conditions and impact load conditions.

**Results** It is demonstrated that there is a strong coupling interaction between PGT and SRM. Under the impact load conditions, the free-vibration mode of the system is excited and the free-vibration modes produced by different components are different. The modal energy method and mode vector distribution are used to diagnose the potential dangerous components of the system. Coupling can effectively suppress the shock oscillation of the system, but it also can increase the interaction effect between the gear system and motor.

**Conclusions** Therefore, the coupling characteristic of the SRM-PGT system should be fully considered, which lays the foundation for the integration design method.

**Keywords** Planetary gear · Switched reluctance motor · Electromechanical dynamic analysis · Integrated drive system

## Abbreviations

SRM Switched reluctance machine  
FEM Finite element method

## List of symbols

$v_{ph}$  Voltage per phase  
 $R_s$  Stator resistance  
 $i_{ph}$  Current per phase  
 $\lambda_{ph}$  Flux linkage per phase  
 $\theta_{ph}$  Mechanical angle per phase  
 $J$  Rotor inertia  
 $\omega$  Mechanical rotational speed  
 $T$  Rotor torque  
 $T_L$  Load torque  
 $B_m$  Rotor damping

$i_j$  ( $j=A, B, C$ ) Current of the  $j$ th phase  
 $L$  Phase inductance  
 $\theta$  Rotor mechanical rotating angle  
 $Wt$  Tooth width  
 $\theta_d$  Angle that the rotor pole deviates from the stator pole  
 $B_{fl}$  Flux density  
 $r$  Radius of the air-gap midcourt line  
 $h$  Stack height  
 $V_{dc}$  Phase coil and the current increases in the coil  
 $\theta_z$  Rigid angular displacement  
 $T_{driving}, T_{driven}$  Driving and driven loads  
 $x, y, z, \theta, k, \text{ and } c$   $x$ -,  $y$ -, And  $z$ -direction displacements, angular displacement, stiffness, and damping  
 $s$  Sun gear  
 $p_n$  Planet gear  $n$   
 $r$  Ring  
 $c$  Planet carrier

✉ Changzhao Liu  
lczcq@qq.com; czliu@cqu.edu.cn

<sup>1</sup> State Key Laboratory of Mechanical Transmission, Chongqing University, Chongqing 400044, China

$f_c$	Carrier rotation frequency
$f_m$	Meshing frequency
$f_e$	Electromagnetic frequency
$f_{mt}$	The frequency components generated by tooth separation
$f_n$	Natural frequency

## Introduction

The switched-reluctance motor (SRM) is an excellent option for motors in electric vehicles, because it is sturdy and has a high starting torque; in addition, it does not require a permanent magnet with rare-earth elements. The rotating speed is improved to increase the power density of the SRM; thus, a reducing gear is needed to adapt to the working conditions. Planetary gear transmission (PGT) is a good option for reducing gears, with the advantages of a large transmission ratio and high power density. Thus, the integration of the SRM and PGT is a future option for power transmission systems in electric vehicles. The dynamic characteristics of the SRM-PGT system should be further investigated, because they have a significant effect on the noise vibration and hardness (NVH) of electric vehicles.

The SRM dynamic model has been widely investigated, and several common dynamic models have been elucidated in [1, 2]. These models focus on the SRM torque calculation, whereas the radial force has a more significant effect on NVH than electromagnetic torque to some extent. To date, some models have been developed to calculate the radial force of the SRM. Yang et al. [3, 4] proposed a model to calculate the SRM radial force based on the magnetic circuit theory when the rotor and stator poles overlap. In this model, the radial force was calculated for three areas: the overlapping area, nonoverlapping area of rotor poles, and nonoverlapping area of stator poles. Husain et al. [5] also proposed a model based on the magnetic circuit theory. In this model, the radial force was calculated for two areas, including the overlapping and nonoverlapping areas of the stator poles. There are three options for calculating the radial force when the stator and rotor poles do not overlap. One approach is to neglect these forces, which are expected to be small. A second approach is to assume that the force is equal to the value computed using the pole overlap model for the rotor position where the pole overlap begins. This estimate is too high. The third approach assumes that there is no saturation without pole overlap.

Many lumped-parameter dynamic models for planetary gears have been proposed. Kahraman [6] proposed a purely torsional model of a single-stage planetary gear set. Tao et al. [7] established the planetary gear system dynamics model and solved the dynamic response of the system by considering various nonlinear factors such as gear meshing

error and clearance. Yang et al. [8] established the dynamics model of helical planetary gear system and comprehensively studied the vibration characteristics of the system. Zhou et al. [9] established the translational torsion dynamics model of planetary gear and studied the effects of roiling frequency, meshing damping, and backlash on bifurcation and chaos characteristics of the system. Qiu et al. [10] established a pure torsional dynamics model for planetary gears and studied the effects of input speed fluctuations and damping on the system parameter instability. Khoozani et al. [11] proposed a three-dimensional lumped mass model of a double-helical planetary gear. Owing to their lightweight design, some planetary gear dynamic models have been proposed considering the flexibility of the ring and carrier. Sun et al. [12] established the rigid-flexible coupling model of planetary gearbox and analyzed the dynamic behavior of inner gear ring. Chen [13] introduced the flexible body into the rigid body dynamics, established the rigid-flexible coupling dynamics model of Marine planetary gear, and analyzed the dynamic response of the system under the failure of broken teeth of the sun gear. Chen [14] carried out dynamics simulation of planetary gear system considering ring gear flexibility and ring gear root crack, respectively. Wu and Parker [15] used Galerkin method and perturbation theory to study the free-vibration frequency and vibration mode of planetary gear transmission system with thin-walled inner gear ring considered, and also studied the dynamic characteristics of planetary gear transmission system with gear ring elasticity considered. Fan and Tatar [16, 17] also introduced a flexible sun shaft and ring gear using the Timoshenko beam and shell theory. In these dynamic models, vibration displacements are used, and the centrifugal force of the carrier is ignored; therefore, it cannot be used for variable and high-speed conditions. Wei et al. [18] proposed a fully coupled dynamic model of planetary gears with a flexible shaft, ring gear, and carrier using virtual beam elements. However, this model ignores the centrifugal forces of the planets and carriers. Wang and Parker [19] developed an analytical dynamic model with the sun, carrier, and planets modeled as rigid bodies coupled to an elastic continuum ring with bending, extensional, and shear deformations. Coriolis and centrifugal accelerations of planets relative to the carrier rotation were included in this model. Therefore, Liu et al. [20] proposed a hybrid model for a flexible helical planetary gear by coupling the lumped-parameter dynamic models for the sun and planets, and flexible for the ring and carrier. And this model can be used in high-speed and nonstationary conditions. Because the angular displacement was used to build the model, it was also convenient to connect with the motor for electromechanical analysis.

Till date, there have been some investigations on the electromechanical dynamic analysis of the motor-planetary gear system. Liu et al. [21, 22] constructed an electromechanical

dynamic model of a drum driving system and investigated the electromechanical dynamic characteristics under shock load and variable speed processes. Bai et al. [23] constructed an electromechanical model that combined a permeance network model of an electric motor and a coupled lateral torsional dynamic model of a planetary gear. The interactions between the motor and gear system were studied. Yi et al. [24, 25] investigated the dynamic interaction behavior of an electric motor drive multistage gear set for the better design and monitoring of gearboxes operating under nonstationary conditions, and found that the vibration frequencies of the multistage gearbox in steady and transient states can be captured in the current, and the electric current can be applied to reflect the external load variation and internal vibration status of the driven gearbox under stationary or nonstationary conditions. In these studies, the lumped-parameter dynamic model was used for the gear system, and the flexibility of the carrier and ring was not considered.

Thus, the SRM dynamic model is constructed first, including the calculation of the radial forces. Then, the dynamic model of the mechanical parts of the SRM-PGT system is built using the reduced-order finite-element method, which considers the flexibility of the components (such as the SRM case, stator, ring gear, and carrier). Based on these, an electromechanical dynamic model is constructed for the SRM-PGT system. Finally, the electromechanical coupling dynamic characteristics and the interaction between the PGT and SRM are investigated, with and without the coupling between the motor and planetary gear under steady-state conditions and impact load conditions.

### Dynamic Model of SRM

The SRM and its parameters are shown in Fig. 1. The universal dynamic model is given by Eq. (1)

$$\begin{cases} v_{ph} = R_s i_{ph} + \frac{d\lambda_{ph}(i_{ph}, \theta_{ph})}{dt} \\ T = \sum_1^3 \left( \int_0^{i_{ph}} \frac{\partial \lambda_{ph}(i_{ph}, \theta_{ph})}{\partial \theta_{ph}} di_{ph} \right) \\ J \frac{d\omega}{dt} = T - T_L - B_m \omega \end{cases} \quad (1)$$

where  $v_{ph}$ ,  $R_s$ ,  $i_{ph}$ ,  $\lambda_{ph}$ , and  $\theta_{ph}$  are the voltage, stator resistance, current, flux linkage, and mechanical angle per phase, respectively.  $J$  represents the rotor inertia,  $\omega$  denotes the mechanical rotational speed,  $T$  denotes the rotor torque,  $T_L$  denotes the load torque, and  $B_m$  represents the rotor damping.

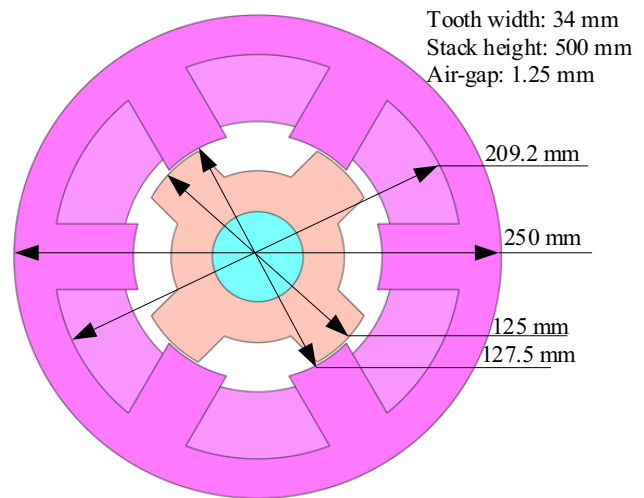


Fig. 1 Switched reluctance machine (SRM) and its Simulink dynamic model from JMAG

For modeling convenience and accuracy, the Simulink dynamic model from JMAG was used for SRM. However, in this model, only the total torque was provided. Therefore, the calculation of the radial and tangential forces on each tooth is given next.

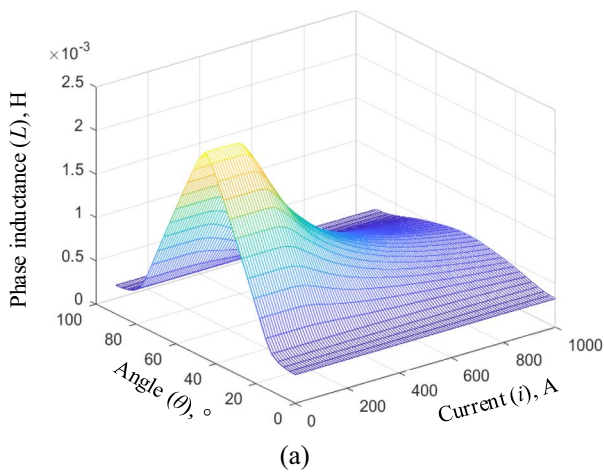
### Decomposition of Torque on Per Phase

The conducting time of the phases of the SRM may overlap, especially when the SRM starts or a large torque is required. The torque in the Simulink model from JMAG contains three phases; thus, it should be deposited in each phase. The torque of each phase ( $T_j$ ) can be obtained using Eq. (2), where  $i_j$  ( $j = A, B, C$ ) is the current of the  $j$ th phase,  $L$  is the phase inductance, and  $\theta$  is the rotor mechanical rotating angle. The phase inductance can be obtained by FEM, and  $L$  and  $dL/d\theta$  are shown in Fig. 2. A comparison of the torque of each phase from the method in this study and FEM is shown in Fig. 3, validating the method of decomposition of torque per phase. Torque spectrum analysis diagram is shown in Fig. 4, and electromagnetic torque waves are mainly based on  $6n$  times of the electrical frequency component

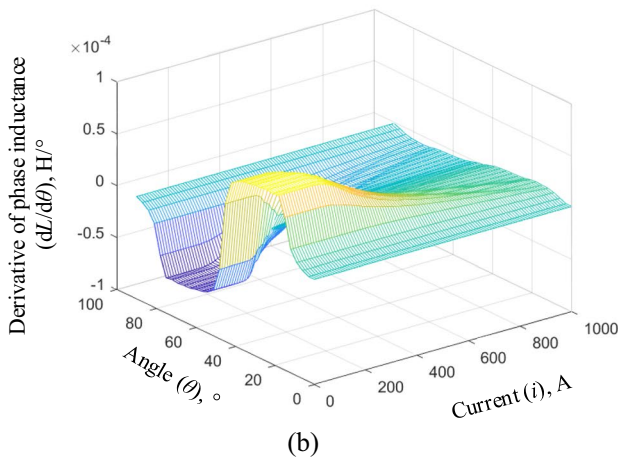
$$T_j = \int_0^{i_j} \frac{\partial L}{\partial \theta} di, \quad j = A, B, C. \quad (2)$$

### Calculation of the Radial Force

The air-gap magnetic flux density is shown in Fig. 5 for the rotor positions where the stator and rotor poles overlap. The magnetic circuit equation for the overlapping and



(a)



(b)

Fig. 2 Phase inductance (L, a) and its derivative (dL/dθ, b)

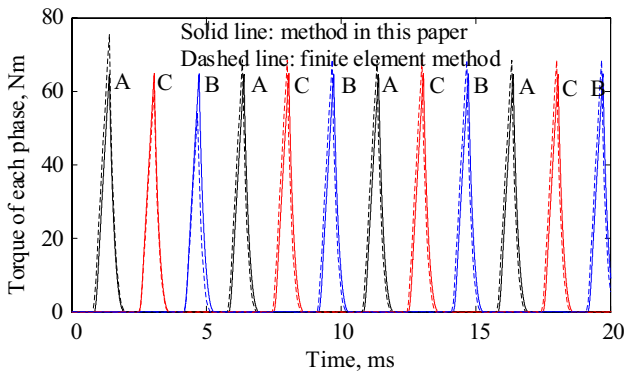


Fig. 3 Comparison of torque of each phase from method in this study and FEM

nonoverlapping parts can be derived using Eqs. (3) and (4), respectively. Because  $B_{f1}$  and  $B_{f2}$  are approximately symmetric [4, 22, 23], only the equation for  $B_{f1}$  is given

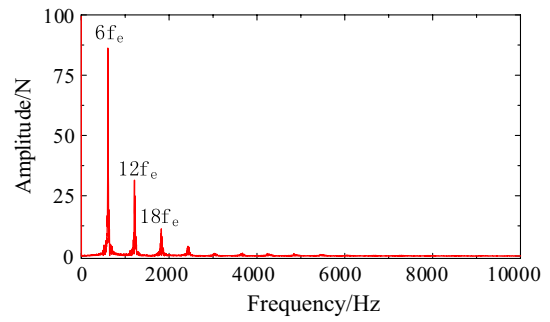


Fig. 4 Torque spectrum analysis

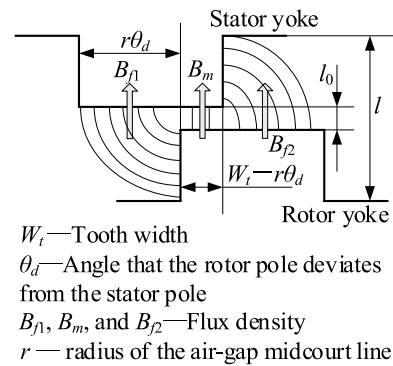


Fig. 5 Air-gap flux density when the stator and rotor poles overlap

$$\begin{cases} Ni = H_g l_0 + H_s(l - l_0) \\ B_m = \mu_0 H_g \end{cases}, \tag{3}$$

$$\begin{cases} Ni = H_{f1} l_{f1} + H_s(l - l_{f1}) \\ B_{f1} = \mu_0 H_{f1} \end{cases}, \tag{4}$$

where  $N$  is the number of turns per coil,  $\mu_0$  is the air permeability,  $i$  is the current,  $H_g$  and  $H_{f1}$  are the magnetic field intensities in the air gap, and  $H_s$  is the magnetic field intensity in the iron core. The relationship between  $H_s$  and  $B_m$  or  $B_{f1}$ , that is, the  $B$ – $H$  curve, is shown in Fig. 6.  $l_{f1}$  can be calculated using Eq. (5) [4, 24]

$$l_{f1} = l_0 + \pi r |\theta_d|/4. \tag{5}$$

Equations (3) and (4) can be solved numerically. The relationship between the magnetic flux density ( $B_m$ ) and current ( $i$ ) is shown in Fig. 7. The relationship between the magnetic flux density ( $B_{f1}$ ), current ( $i$ ), and deviation angle ( $\theta_d$ ) is shown in Fig. 8. Thus, the radial force when the rotor and stator poles overlap can be calculated using Eq. (6) [26], where  $h$  denotes the stack height

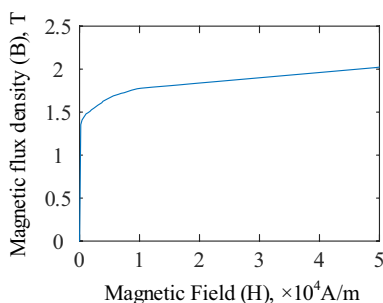


Fig. 6 B–H curve

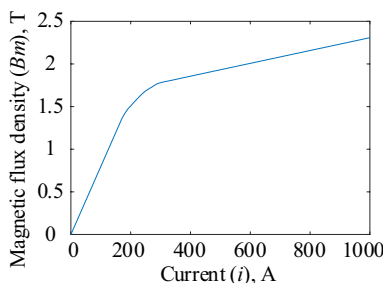


Fig. 7 Relationship between magnetic ( $B_m$ ) and current ( $i$ )

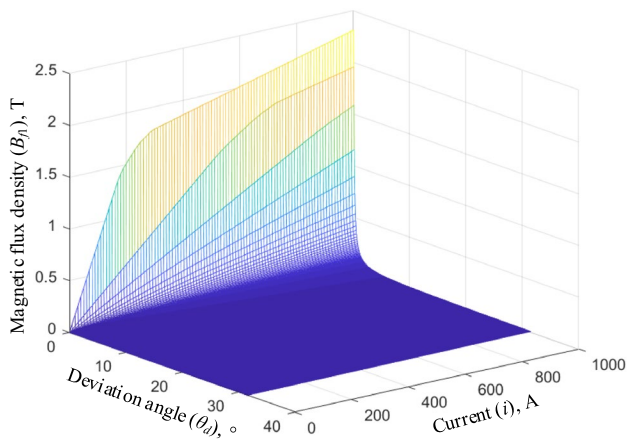


Fig. 8 Relationship between magnetic flux density ( $B_{fl}$ ), current ( $i$ ), and deviation angle ( $\theta_d$ )

$$F_{\text{roverlap}} = \frac{h}{2\mu_0} (B_m^2 (Wt - r\theta_d) + 2B_{fl}^2 r\theta_d). \tag{6}$$

As described in [25], there are three options for calculating the radial force for rotor positions where the stator and rotor poles do not overlap. One approach is to neglect these forces, which are expected to be small. This estimate is obviously low. The second approach is to assume that the force is independent of the rotor position and is equal

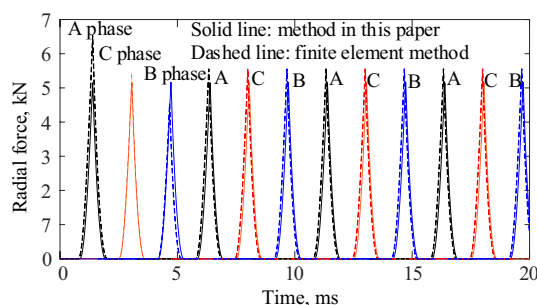


Fig. 9 Comparison of radial forces from method herein and FEM

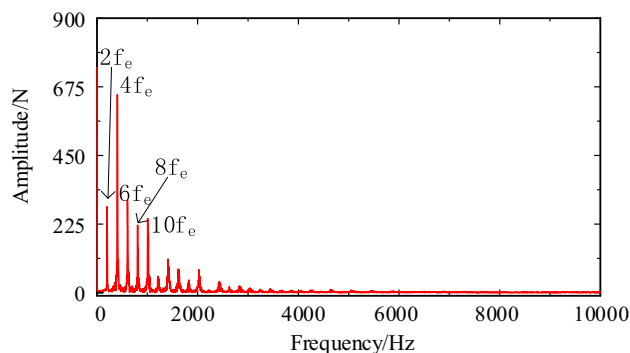


Fig. 10 Radial force spectrum analysis

to the value computed using the pole overlap model for the rotor position where pole overlap begins. This estimate is too high. The third approach assumes that there is no saturation without pole overlap. In this study, the third approach was chosen. The radial force when the stator and rotor poles do not overlap is calculated using Eq. (7) [27, 28], where  $L_u$  and  $l_{u0}$  are the inductance of one pole and the air-gap length, respectively, when the rotor and stator poles are unaligned

$$F_{\text{rnonoverlap}} = \frac{1}{2} i^2 \frac{L_u}{l_{u0}}. \tag{7}$$

The comparison of radial forces from the method in this study and the FEM is shown in Fig. 9, where the turn-on and turn-off angles are  $15^\circ$  and  $25^\circ$ , respectively, the rotating speed is 3000 rpm, and the voltage is 400 V. The radial forces are very close for the method in this study and FEM, thus validating the method proposed herein. Radial force spectrum analysis diagram is shown in Fig. 10, and electromagnetic radial force waves are mainly based on  $2n$  times of the electrical frequency component.

### Control System of SRM

The converter circuits of the SRM are shown in Fig. 11. When the thyristor is turned on,  $V_{dc}$  is applied to the phase



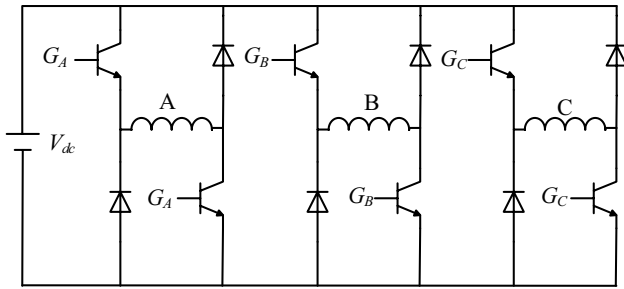


Fig. 11 Converter circuits of the SRM

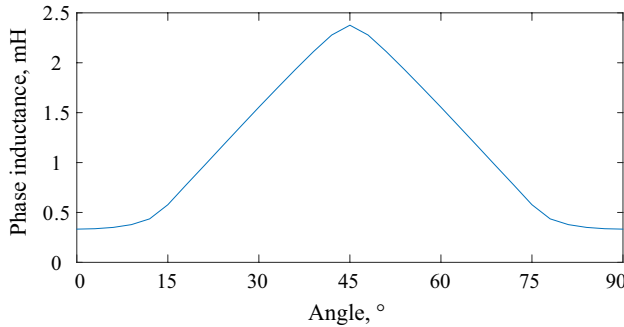


Fig. 12 Phase inductance when the current is 100 A

coil and the current increases in the coil. When the thyristor is turned off, a negative  $V_{dc}$  is applied to the phase coil and the current decreases in the coil. Therefore, the current in the coil can be controlled by the gate signal of the thyristor. When the coil is conducting in the increasing region of inductance in Fig. 12, a positive torque can be obtained. When the coil is conducting in the decreased region of inductance in Fig. 12, a negative torque can be obtained. The larger the coil current, the larger is the torque [29]. In this study, the turn-on and turn-off angles are fixed and the coil current is adjusted to change the torque when the speed is low. Figure 13a shows the current with a rotating speed of 3000 rpm. The turn-on and turn-off angles are adjusted to change the torque when the speed is high. Figure 13b shows the current with a rotating speed of 15,000 rpm. When starting, current control is used, but the conducting angle should be sufficiently long to make the current overlap between phases. A schematic diagram of the control is shown in Fig. 14.

### Dynamic Model of Mechanical Parts

The switched-reluctance motor-planetary gear system (SRM-PGT system) is shown in Fig. 15. The two configurations are analyzed herein. There is no coupling between the rotor and sun gear, as shown in Fig. 15a, while there is

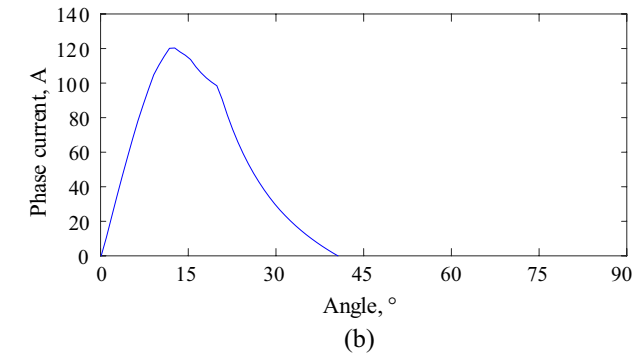
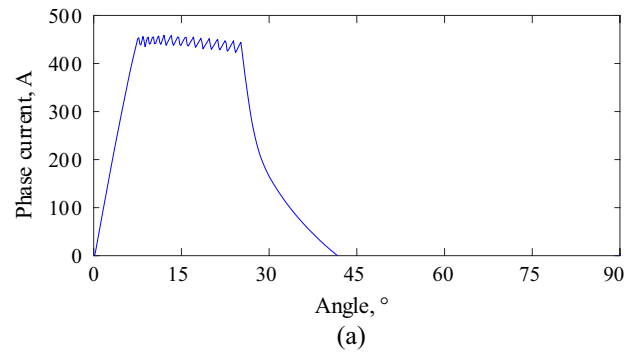


Fig. 13 Phase current of current control (a) and angle control (b)

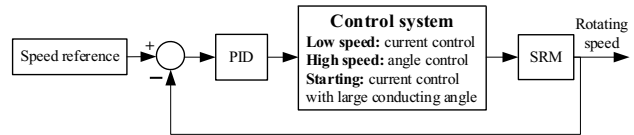


Fig. 14 Control schematic diagram of SRM

a coupling, as shown in Fig. 15b. To improve the computational speed, finite-element (FE) models were constructed and then reduced for dynamic models of mechanical parts. The stator, rotor, motor case, ring gear, and carrier are modeled using the reduced FE method, whereas the gear is modeled by the lumped-parameter method.

### Reduced-Order Finite-Element model

The equations of motion for a dynamic system are expressed by Eq. (8), where  $\mathbf{M}$ ,  $\mathbf{C}_d$ , and  $\mathbf{K}$  are the mass, damping, and stiffness matrices, respectively;  $\mathbf{u}$  is the displacement vector; and  $\mathbf{F}$  is the load vector

$$\mathbf{M}\ddot{\mathbf{u}} + \mathbf{C}_d\dot{\mathbf{u}} + \mathbf{K}\mathbf{u} = \mathbf{F}. \tag{8}$$

According to the orthogonality of the model coordinates, Eq. (8) can be transformed into a modal coordinate system with  $n$  dof decoupled equations, as shown in Eq. (9), where

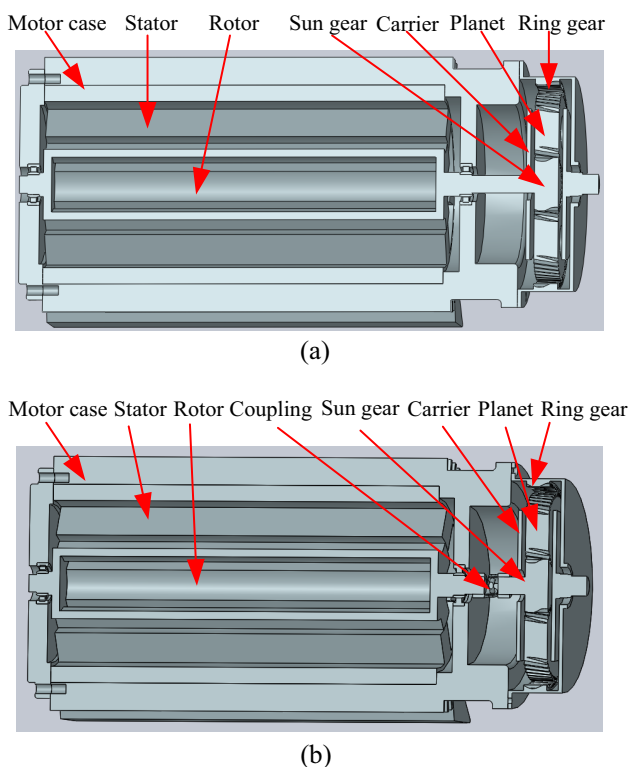


**Fig. 15** Switched reluctance motor-planetary gear system (SRM-PGT system)

ndof is the total degrees of freedom (DOFs) of the dynamic system,  $\Phi_j$  is the  $j$ th mode shape vector, and  $y_i$  is the set of modal coordinates

$$\ddot{y}_j + 2\xi_j \omega_j \dot{y}_j + \omega_j^2 y_j = \Phi_j^T \mathbf{F} \quad j = 1, 2 \dots \text{ndof}. \tag{9}$$

High-order modes usually have a limited effect; therefore, the preceding  $n$  equations in Eq. (9) can be solved for a system dynamic analysis to reduce the computational effort. The preceding  $n$  equations in Eq. (9) are second-order differential equations, which can be transformed into the following state equation:

$$\begin{cases} \dot{\mathbf{z}} = \mathbf{A}\mathbf{z} + \mathbf{B}\mathbf{F}_s \\ \mathbf{v} = \mathbf{C}\mathbf{z} + \mathbf{D}\mathbf{F}_s \end{cases} \tag{10}$$

where

$$\mathbf{z} = \begin{bmatrix} \mathbf{y} \\ \dot{\mathbf{y}} \end{bmatrix}, \mathbf{v} = \begin{bmatrix} \mathbf{w} \\ \dot{\mathbf{w}} \end{bmatrix}.$$

In particular,  $\mathbf{w}$  is the displacement vector of the observed DOFs;  $\mathbf{y}$  is the modal coordinate vector;  $\mathbf{A}$ ,  $\mathbf{B}$ ,  $\mathbf{C}$ , and  $\mathbf{D}$  are the matrices of the state equation; and  $\mathbf{F}_s$  is the input force vector.

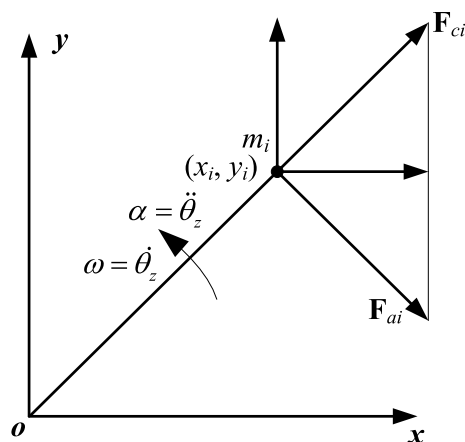


**Fig. 16** Inertia force, centrifugal force, and Coriolis force of the node  $i$

### Inertia and Centrifugal Forces of the Mechanical Parts with Rigid Rotation

The inertia and centrifugal forces should be added to the reduced-order model because of the rigid rotation of the rotor and carrier. The effect of the Coriolis force is not significant, and the computational speed is slow when the Coriolis force is added; hence, the Coriolis forces are ignored [16]. As shown in Fig. 16,  $(x_i, y_i)$  is the coordinate of node  $i$  in the moving coordinate system  $oxyz$ , where  $m_i$  is the mass of node  $i$ ;  $\mathbf{F}_{ai}$  and  $\mathbf{F}_{ci}$  are the inertia and centrifugal forces of node  $i$ , respectively;  $\theta_z$ ,  $\omega$ , and  $\alpha$  are the rigid angular displacement, velocity, and acceleration, respectively.

The inertia force of node  $i$  is derived as Eq. (11)

$$\mathbf{F}_{ai} = \begin{bmatrix} m_i y_i \\ -m_i x_i \\ 0 \end{bmatrix} \alpha. \tag{11}$$

The inertia forces of all the nodes should be transformed to modal coordinates to be applied to the carrier reduced-order model, as shown in Eq. (12)

$$\mathbf{F}_{aq} = \Phi^T \mathbf{F}_a = \Phi^T \begin{bmatrix} m_i y_i \\ -m_i x_i \\ 0 \\ \dots \end{bmatrix} \alpha. \tag{12}$$

The centrifugal force of node  $i$  is derived as Eq. (13)

$$\mathbf{F}_{ci} = \begin{bmatrix} m_i x_i \\ m_i y_i \\ 0 \end{bmatrix} \omega^2. \tag{13}$$

The centrifugal forces of all nodes should be transformed to modal coordinates, as shown in Eq. (14)

$$F_{cq} = \Phi^T F_c = \Phi^T \begin{bmatrix} m_i x_i \\ m_i y_i \\ 0 \\ \dots \end{bmatrix} \omega^2. \tag{14}$$

### Reduced-Order FE Model of Rotor

The rotor is illustrated in Fig. 17. Four concentrator nodes are built. Concentrator nodes 1 and 2 were attached to the bearing journal. Concentrator Node 3 was attached to the rotor surface. Concentrator node 4 is attached to the sun gear without teeth for the configuration without coupling, as

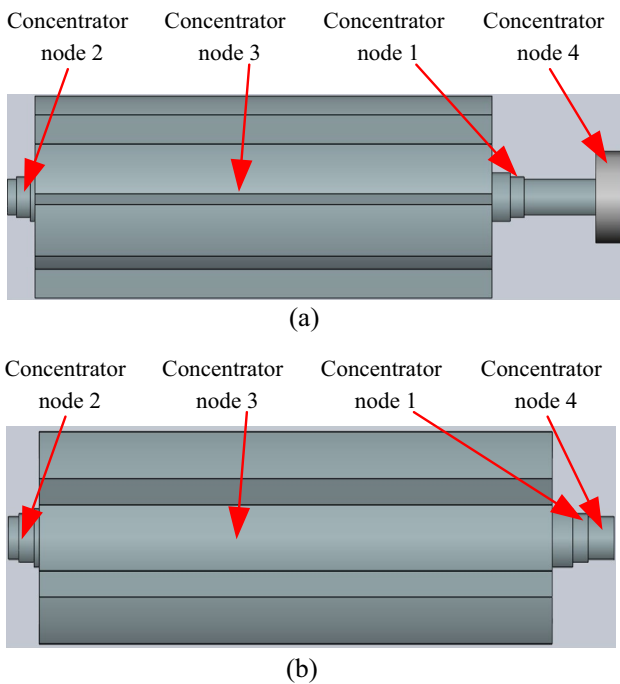
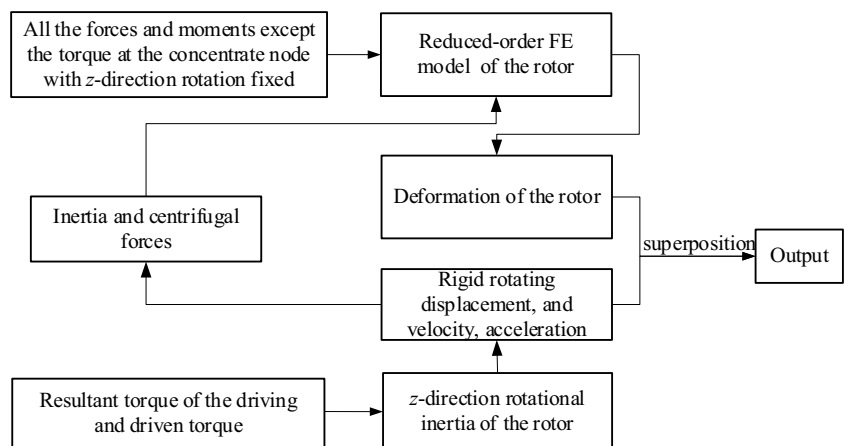


Fig. 17 Rotor of SRM

Fig. 18 Complete reduced-order model of the rotor



shown in Fig. 17a, while concentrator node 4 is attached to the journal for the configuration with coupling, as shown in Fig. 17b. The  $z$ -direction rotation of concentrator node 4 is fixed. The rigid angular displacement, velocity, and acceleration of the rotor can be obtained using Eq. (15)

$$J_z \ddot{\theta}_z = T_{driving} - T_{driven}, \tag{15}$$

where  $\theta_z$  is the rigid angular displacement, and  $T_{driving}$  and  $T_{driven}$  are the driving and driven loads, respectively. The drive load is the electromagnetic torque acting on the rotor, while the driven torque is the torque acting on the sun gear or coupling for the configuration with and without coupling. The complete reduced-order model of the rotor is shown in Fig. 18.

### Reduced-Order FE Model of the Assembly of Stator, Case, and Ring Gear

The connection of the stator and motor case is an interference fit, and the case and ring gear are connected fixedly by bolts. To simplify the modeling process, the stator, case, and ring gear are regarded as assemblies. As shown in Fig. 19, the concentrator nodes 1–125 were attached to the ring gear teeth. Concentrator node 126 was attached to the bearing journal of the ring gear. Concentrator nodes 127–128 were attached to the bearing journal of the motor case. Concentrator nodes 129–134 were attached to the stator teeth. The reduced-order FE model of the assembly can be obtained using the method described in Sect. Reduced-order Finite-Element Model.

### Hybrid Dynamic Model of the Planetary Gear

The dynamic model of a helical planetary gear is illustrated in Fig. 20. There are three types of coordinate systems: (1) the static coordinate system  $OXYZ$ , (2) the moving



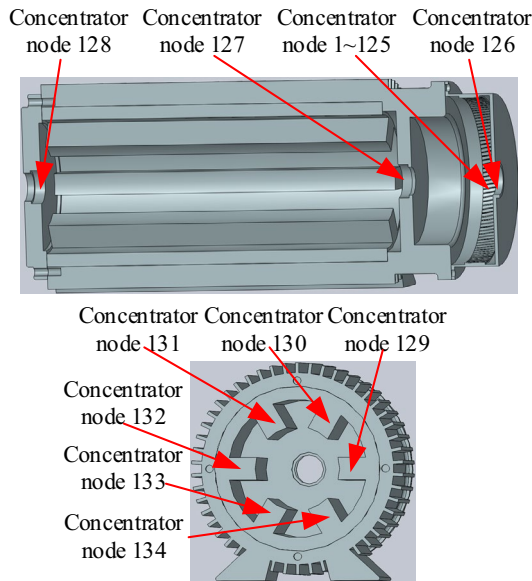


Fig. 19 Stator, case, and ring gear

coordinate system  $oxyz$  rotating with the carrier, and (3) the moving coordinate system  $o_{pn}x_{pn}y_{pn}z_{pn}$  ( $n = 1 \dots N$ , where  $N$  is the number of planets) rotating with the carrier. The symbols  $x, y, z, \theta, k$ , and  $c$  represent the  $x$ -,  $y$ -, and  $z$ -direction displacements, angular displacement, stiffness, and damping, respectively. The subscripts  $x, y, z, s, r, pn$ , and  $c$  represent the  $x$ -,  $y$ -, and  $z$ -directions, sun, ring,  $n$ th planet, and carrier, respectively. The subscripts  $t$  and  $c$  represent the torsional stiffness and damping, respectively. To obtain the dynamic model of the sun and planets, the helical planetary gear set is first transformed into parallel-axis external and internal gear pairs in the moving coordinate system to obtain the meshing forces. Subsequently, Newton’s law in

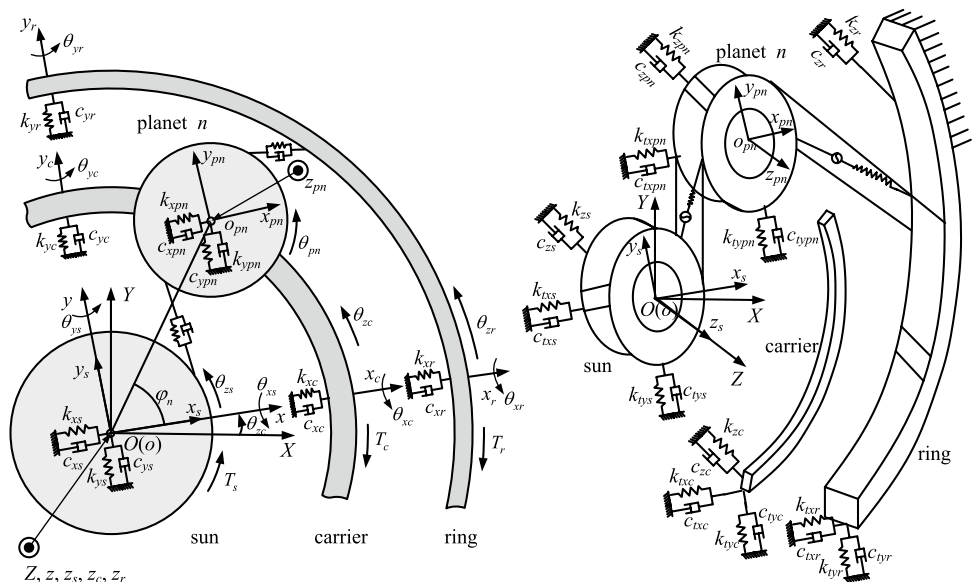
a non-inertial coordinate system is utilized to obtain the equations of motion of the sun and planets. The dynamic models of the carrier and ring gears are obtained by the reduced-order FE method. The lumped-parameter dynamic model of the sun and planets, as well as the reduced-order FE model of the ring and carrier, can be coupled for the hybrid dynamic model of the planetary gear, as described in Ref. [20] in detail. The parameters of the planetary gear are given in ref [20].

Before the simulation, the meshing stiffness was obtained with finite-element software. The meshing stiffness values of the sun–planet and planet–ring gear pairs during the meshing period are given in Fig. 21.

### Dynamic Model of the SRM-PGT System

The dynamic model of the SRM and mechanical parts can be coupled to the dynamic model of the SRM-PGT system, as shown in Fig. 22. The dynamic model of the SRM provides the radial force acting on the stator and the radial force and electromagnetic torque on the rotor. The dynamic model of the rotor provides the rotor angular displacement and velocity for the dynamic model of the SRM. The dynamic model of the rotor also provides the angular displacement and velocity of the sun for the hybrid dynamic model of the planetary gear. The hybrid dynamic model of the planetary gear provides the force and moment at the concentrator node 4 of the rotor. The hybrid dynamic model of the planetary gear and the dynamic model of the assembly of the stator, case, and ring are coupled through a ring gear, as described in Ref. [20], in detail.

Fig. 20 Dynamic model of the helical planetary gear set



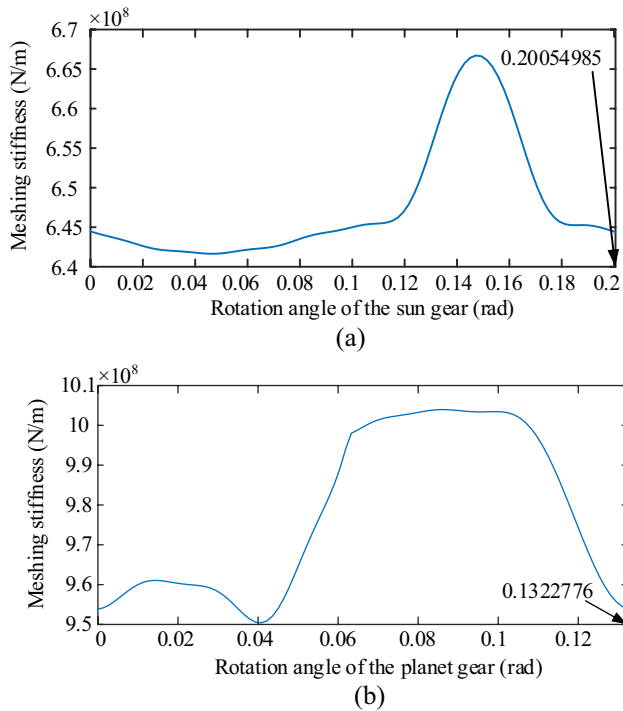


Fig. 21 Meshing stiffness of the **a** sun–planet and **b** planet–ring gear pairs

### Simulation and Analysis

The operating conditions of the system are shown in Fig. 22. The reference speed of the electric motor was 3000 rpm. A constant load of  $-500$  N was applied in the range of  $0-1.1$  s. The impact load was applied at  $1.1$  s and ended at  $2.1$  s, changing from  $-500$  N to  $500$  N. During  $1.1-2.1$  s, the electric vehicle is in a downhill state. The rotation speed of the motor during the entire simulation process is shown in Fig. 23. The system motion process is mainly divided into three stages. The first stage is the starting process of the system at  $0-0.1$  s, and the motor speed starts from  $0$  rad/s to the rated speed  $314$  rad/s. The second stage is the steady-state process in which the system maintains the rated speed

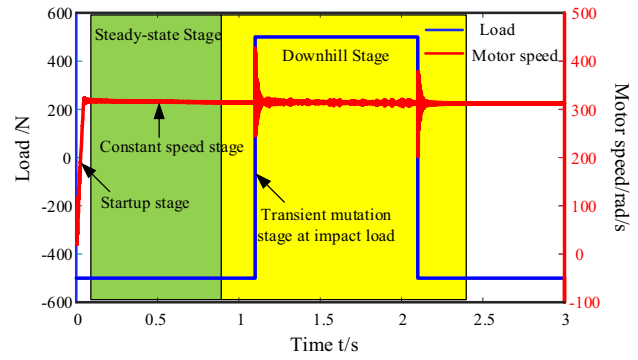


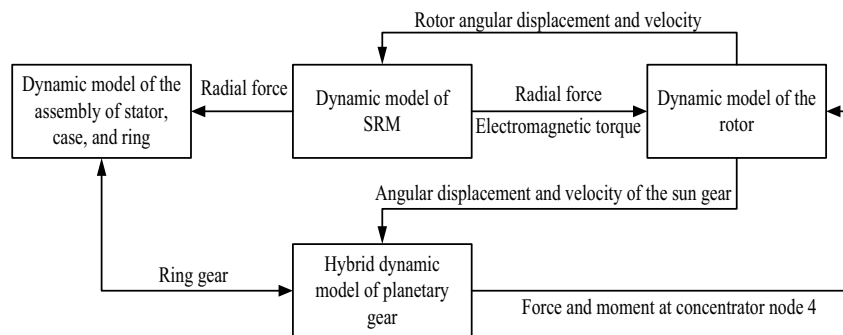
Fig. 23 SRM-PGT system load and motor speed

under the action of the speed control, such as,  $0.55-0.75$  s; the third stage is the unsteady state stage when the speed under the action of sudden load at  $1.1$  s and  $2.1$  s. An electro-mechanical dynamic analysis was conducted for the SRM-PGT system with and without coupling in the steady and transient states.

### Steady-State Dynamics Analysis

The steady-state stage ( $0.5-0.75$  s) was chosen to analyze the dynamic characteristics of the RSM-PGT system. During this period, the load on the system was  $-500$  N m, and the motor speed was  $3000$  rpm. Figure 24 shows the time-domain (a) and frequency-domain (b) dynamic meshing forces of the planet–ring pair with and without coupling. As shown in Fig. 24a, the minimum value of the dynamic meshing force is zero, which indicates that the tooth surface separation phenomenon occurs. The coupling has little effect on the dynamic meshing force of the planet–ring gear pair. As shown in Fig. 24b, the rotation frequency of the carrier  $f_c$ , the meshing frequency  $f_m$ , and the electromagnetic excitation frequencies  $4f_e$  and  $6f_e$  can be found in the low-frequency region.  $f_e$  is the fundamental frequency of the motor,  $f_e = p\omega_r / 2\pi$ . The energy of the frequency component

Fig. 22 Flowchart of the hybrid dynamic modeling



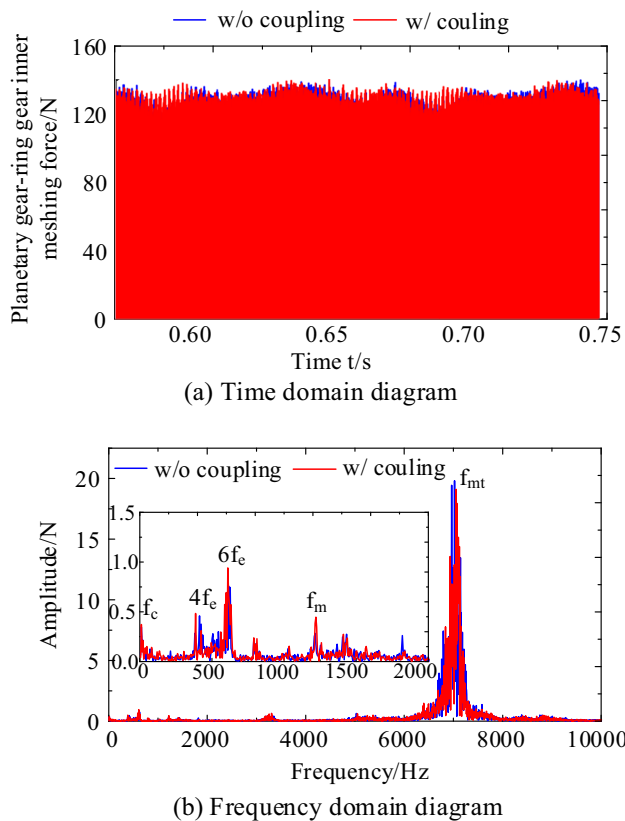


**Fig. 24** Time-domain (a) and frequency spectrum (b) dynamic meshing force of the planet–ring pair with and without coupling

( $f_{mt}$ ) in the high-frequency region is the largest in the frequency spectrum, which is caused by tooth separation. The frequency component ( $f_{mt}$ ) in Fig. 25 is caused by excitation from the planet–ring dynamic meshing force and much smaller when there is no teeth separation for the sun-planet dynamic meshing force, as shown in Figs. 24 and 25.

Figure 25 depicts the time-domain (a) and frequency-domain (b) sun-planet dynamic meshing force with and without coupling. As shown in Fig. 25a, the coupling has no effect on the average meshing force of the sun-planet gear pair, but it has a small effect on the fluctuation amplitude of dynamic meshing force. When there is a coupling, the dynamic meshing force fluctuates slightly. From Fig. 25b, it can be seen that the multiplication of carrier rotation frequency ( $3f_c$ ) and the multiplication of meshing frequency ( $f_m$  and  $2f_m$ ) in the gear system appears in the low-frequency region. It also contains electromagnetic frequency components ( $6f_e$  and  $18f_e$ ) of the motor, and the amplitude of the frequency component of  $6f_e$  is the largest. Therefore, the sun-planet meshing force is mainly affected by the electromagnetic excitation frequency which from the motor. The high-frequency region primarily contains the frequency components ( $f_{mt}$ ) generated by tooth separation. When there is a coupling, the amplitude of  $6f_e$  in the meshing force

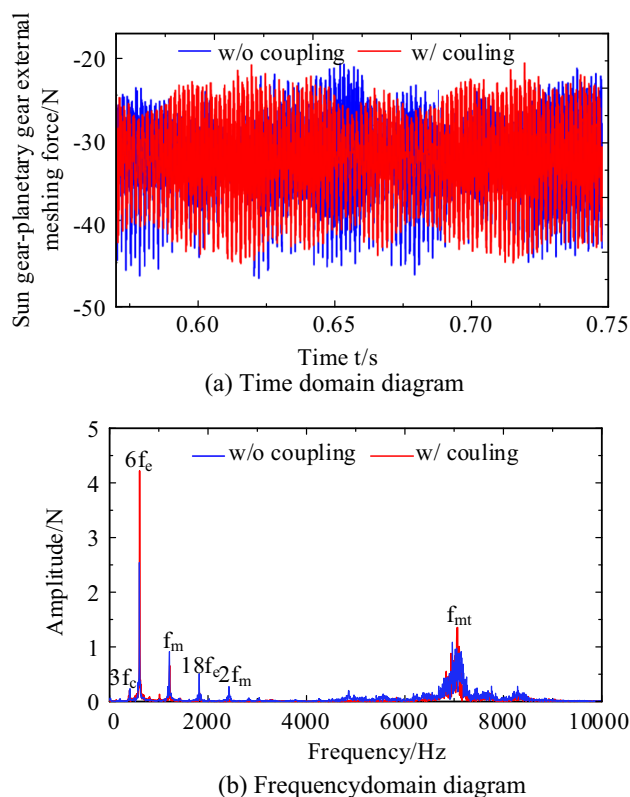


**Fig. 25** Time-domain (a) and frequency-domain (b) sun-planet dynamic meshing force with and without coupling

increases, reflecting stronger coupling effect of the gear and motor system.

The NVH of electric vehicle driving systems has received extensive attention from designers. Figure 26 shows the time-domain (a, b) and frequency-domain (c, d) plots of the vibration displacement in the X and Y directions at the ring gear tooth with or without coupling. As shown in Fig. 26a, b, the coupling has no effect on the mean value of the radial vibration displacement at the ring gear teeth, but it has a minor effect on the vibration amplitude. When there is no coupling, the vibration amplitude of the gear teeth is slightly smaller. In Fig. 26c, d, the vibration displacement of the ring gear mainly contains multiplication of the carrier frequency ( $3f_c$ ), disengagement frequency ( $f_{mt}$ ), and 2, 4, and 6 times the electromagnetic excitation frequency. Among them, the electromagnetic excitation frequency has the largest amplitude and plays a leading role. Therefore, for the integrated drive system of the RSM-PGT, the vibration characteristics of the ring teeth are mainly affected by the electromagnetic excitation frequency. The frequencies of  $2f_e$  and  $4f_e$  are from the electromagnetic radial force that acts on the stator and transmits to the ring through the case. Therefore, reducing the fluctuation of the electromagnetic radial force can effectively reduce the vibration of the gearbox. When there is a coupling, the energy of the electromagnetic excitation

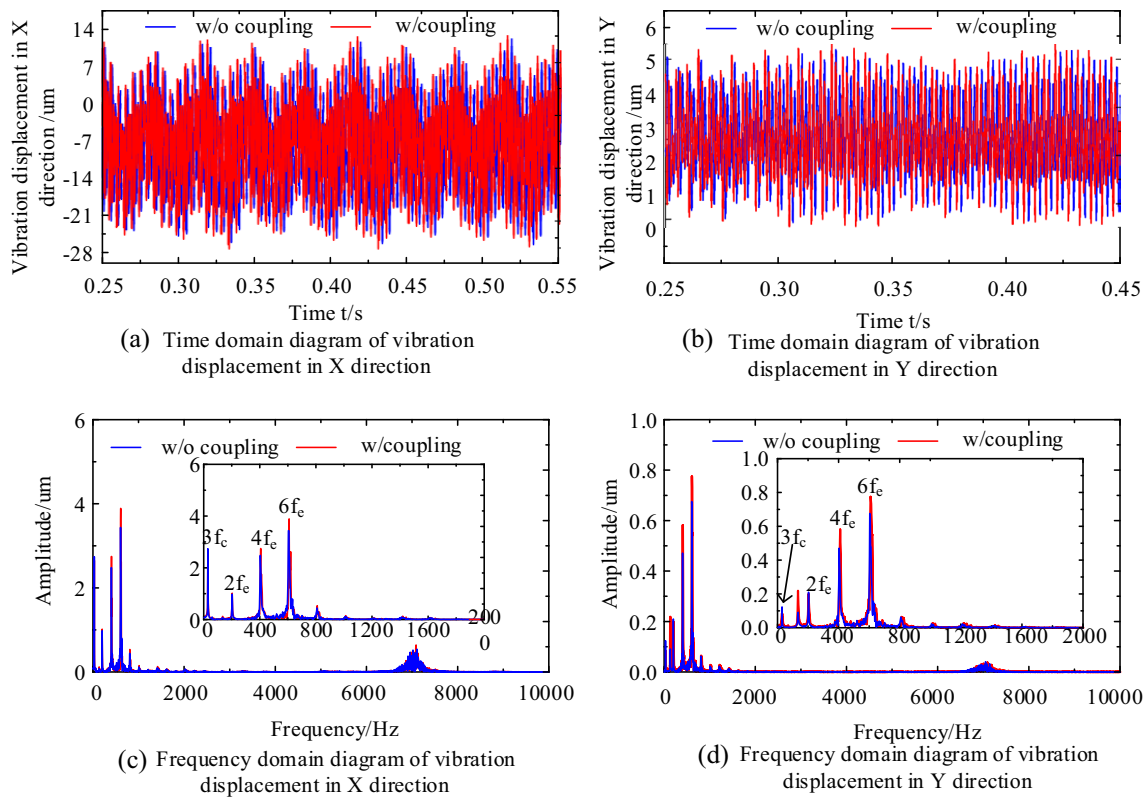


**Fig. 26** Time-domain (a, b) and spectrum (c, d) of the vibration displacement in the X and Y direction at the ring gear tooth with or without coupling

frequency in the vibration displacement of the ring tooth is obviously increased, which enhances the electromechanical interaction effect of the system.

Figure 27 shows the bearing reaction force on the motor side (a) and its frequency spectrum (b) with and without a coupling. From Fig. 27a, it can be seen that the coupling has no effect on the mean value of the bearing reaction force on the motor side, and mainly affects the fluctuation amplitude of the bearing reaction force. When there is no coupling, the fluctuation amplitude of the radial reaction force is smaller. As illustrated in Fig. 27b, in the low-frequency region, the rotation frequency of carrier ( $f_c$ ) and the electromagnetic excitation frequency of the SRM have been appeared in the form of  $n \cdot f_c \pm m \cdot f_e$ . The carrier frequency is electromagnetic excitation frequency from the SRM ( $4f_e, 6f_e$ ), the modulation frequency is rotation frequency of carrier ( $f_c$ ). There are more kinds of modulation frequencies in the signals without a coupling, just like  $4 \cdot f_e \pm 6 \cdot f_c, 6 \cdot f_e \pm 6 \cdot f_c$ . The bearing radial support reaction fluctuation of the motor side is mainly affected by the electromagnetic radial force.

Figure 28 shows the time-domain (a) and frequency spectrum (b) of the radial vibration acceleration at the stator core teeth of SRM with or without coupling. It can be seen from Fig. 28a that when there is no coupling, the vibration

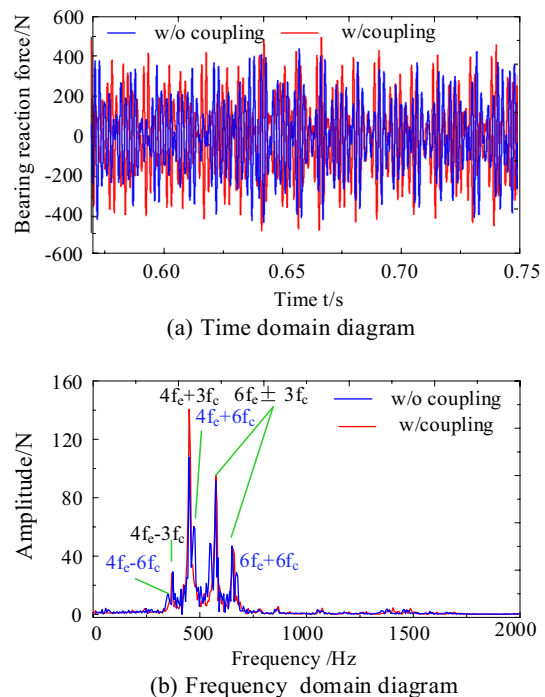


**Fig. 27** Time-domain (a) and frequency spectrum (b) of the bearing reaction force on the motor side with or without a coupling

acceleration fluctuation at the stator core teeth of the motor is smaller. It can be seen from Fig. 28b that the main frequency components include the electromagnetic excitation frequency of the motor ( $6f_e$ ,  $8f_e$ , and  $20f_e$ ), multiplication of the meshing frequency of the planetary gear system ( $2f_m$  and  $3f_m$ ), and the frequency  $f_{mt}$  generated by tooth surface separation. When there is a coupling, the energy of the gear system excitation frequency ( $2f_m$ ,  $3f_m$ , and  $f_{mt}$ ) is increased, which strengthens the influence of the gear system on the vibration characteristics of the motor. At the same time, the 24th order natural frequency  $f_{n24}$  appears with the largest energy, which plays a leading role. At this time, the  $f_{n24}$  is consistent with meshing frequency of planetary gear.

In summary, the dynamic characteristics of the gear system are affected not only by its own internal excitation, but also by the electromagnetic excitation of the motor. The electromagnetic radial force in the motor fluctuates significantly, which has a significant impact on the vibration characteristics of the gear system. Simultaneously, the dynamic characteristics of the SRM are also affected by the excitation of the gear system. For the integrated RMS-PGT driving system, reducing the radial force fluctuation of the SRM and solving the phenomenon of meshing tooth surface separation will help to

reduce the vibration of the system. Meanwhile, the coupling has a small effect on the dynamic characteristics of the gear side, but it has a significant effect on the vibration characteristics of the motor side. When there is coupling, the coupling characteristics of the motor and gear system are enhanced.

### System Natural Frequency Analysis

In this study, the SRM-PGT system is a vibration system with general viscous damping; therefore, complex modal analysis needs to be conducted. The vibration differential equation of the system is

$$M\ddot{x} + C\dot{x} + Kx = f(t), \tag{16}$$

where  $M$  is the mass matrix,  $K$  is the stiffness matrix, and  $C$  is the damping matrix. In a complex modal analysis, the above equation must be transformed into a state equation. The auxiliary Eq. (17) is introduced to form an eigenvector with weighted orthogonality of  $M$ ,  $K$ , and  $C$

$$M\dot{x} - M\dot{x} = 0. \tag{17}$$

The equation is as follows:  $Px' - Qx' = f'(t)$  where:  $x' = \begin{bmatrix} x \\ \dot{x} \end{bmatrix}$ ,  $2n$  order state vector;  $f'(t) = \begin{bmatrix} f(t) \\ 0 \end{bmatrix}$ ,  $2n$  order force vector;  $P = \begin{bmatrix} C & M \\ M & 0 \end{bmatrix}$ ,  $2n \times 2n$  order symmetric matrix, positive definite;  $Q = \begin{bmatrix} K & 0 \\ 0 & -M \end{bmatrix}$  and  $2n \times 2n$  order symmetric matrix, positive definite, or semi-positive definite.

In the formula, let  $f'(t)=0$ , the complex eigenvalues and complex eigenvectors of the system can be obtained. Complex eigenvalues exist in conjugate pairs corresponding to the conjugate eigenvectors. The system damping matrix cannot be diagonalized by the same transformation as the mass and stiffness matrix; hence, the eigenvalues with zero imaginary part will appear, and these eigenvalues are not given in Table 1. The real-valued eigenvalues determine the damping of the system and reflect the attenuation ability. The imaginary part of the eigenvalue represents the natural frequency of the system. The eigenvalues of each order are shown in Table 1 by converting the imaginary unit from rad/s to Hz. The solved eigenvalues are mainly used to discriminate the free-vibration modes in the transient analysis.

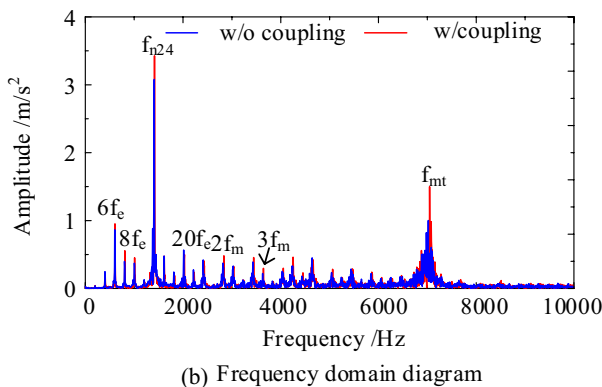
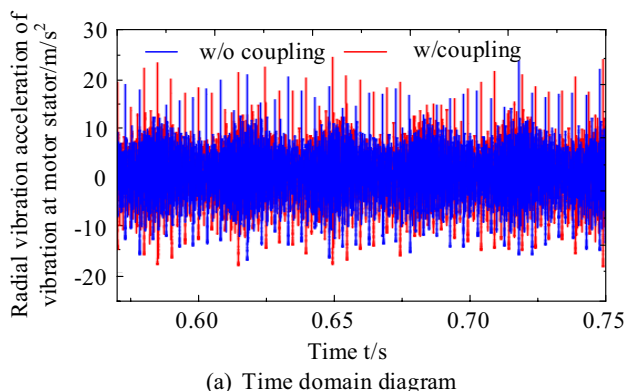


**Fig. 28** Time-domain (a) and frequency spectrum (b) of the radial vibration acceleration at the stator core teeth of SRM with or without coupling

### Transient State Dynamics Analysis

Figure 29 shows the radial vibration characteristics of the ring gear teeth with and without coupling under the impact load of the system. In the steady-state stage, the system



**Table 1** Natural frequency

Order	Eigenvalue	Order	Eigenvalue	Order	Eigenvalue
1	$-0.7793 \pm 111.257i$	8	$-10.005 \pm 454.987i$	15	$-61.944 \pm 887.444i$
2	$-5.337 \pm 112.1982i$	9	$-21.781 \pm 575.254i$	16	$-59.843 \pm 894.793i$
3	$-1.065 \pm 135.7717i$	10	$-107.43 \pm 609.30i$	17	$-57.917 \pm 980.203i$
4	$-2.239 \pm 169.093i$	11	$-32.597 \pm 698.755i$	18	$-59.274 \pm 993.073i$
5	$-10.992 \pm 415.072i$	12	$-27.601 \pm 783.898i$	19	$-59.049 \pm 996.076i$
6	$-10.043 \pm 417.761i$	13	$-29.027 \pm 791.335i$	20	$-70.231 \pm 1065.371i$
7	$-9.645 \pm 440.567i$	14	$-41.115 \pm 837.789i$	21	$-70.284 \pm 1067.827i$

remains in a forced vibration mode produced by electromagnetic excitation frequencies ( $2f_e$ ,  $4f_e$ ,  $6f_e$ ). The system remained in a transient free-vibration mode when it was subjected to an impact load of 1.1 s. The free vibration is gradually attenuated under the action of damping, and the transmission system maintains a steady-state forced vibration. In the downhill process, the peak value of the radial vibration fluctuation at the ring teeth with coupling is greater than that without coupling. It can be seen from the spectrogram that the third-order free-vibration mode ( $f_{n3}$ ) of the system is excited under the transient impact. When there is no coupling, the free-vibration frequency mode energy is larger.

The main components of the SRM-PGT system are the planet gear, carrier, motor rotor (including sun gear), and case (including inner gear ring and motor stator). Figure 30a shows the vibration energy proportion of each component in the third mode. The percentage of vibration energy of the case is up to 90.24%, which is the main vibration component. Figure 30b shows the proportion of the vibration energy at each component under different DOFs. Among them, the vibration at the torsion degree of freedom in the X direction ( $\theta_x$ ) and the torsion degree of freedom in the Y direction ( $\theta_y$ ) of the housing has the highest energy proportion, which is 48% and 49%, respectively. Figure 29c shows the mode vector diagram of the torsion degree of freedom in the X direction ( $\theta_x$ ) at each concentrator node of the case. The position represented by each node number is shown in Fig. 17, which is mainly composed of the ring gear tooth node, bearing hole concentrator node, and motor stator node. The amplitude of the vibration vector at the ring gear teeth is the largest; hence, the main vibration mode of the third natural frequency is the bending mode of vibration in the case, and the main vibration position is each tooth of the ring gear. According to the vibration displacement vector of each tooth of the ring, using the bolt to restraint at the position can help to reduce the bending phenomenon of the third natural frequency free-vibration mode.

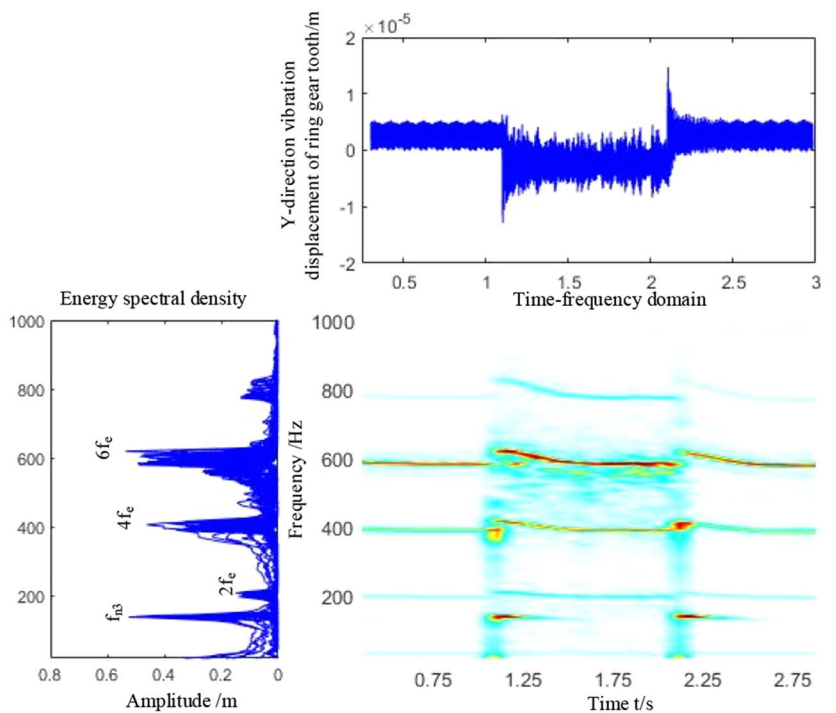
Figure 31 shows the time–frequency diagram of the sun-planet meshing force with and without coupling. When there is a coupling, the meshing impact of the dynamic meshing force under the impact load is smaller. Therefore, the coupling plays a role in reducing the meshing impact at the sun–planet gear pair. In the steady state, the main excitation frequency of the sun–planet gear meshing force is the electromagnetic excitation frequency of the motor ( $6f_e$ ). During the transient process, the sixth-order and third-order free-vibration modes of the system are excited, and the sixth-order mode has a larger frequency energy.

Figure 32 shows the vibration vector distribution diagram of the sixth-order free-vibration mode excited by the system under the impact load. Figure 32a shows the distribution of each sub-structure component vibration energy. The percent of energy is mainly concentrated in the case, carrier and planet gear, and respectively, accounted for 33.97%, 34.3%, and 31.47%. Combined with Fig. 32b, it can be seen that the vibration energy at the torsion degree of freedom in X direction ( $\theta_x$ ) accounts for the largest proportion. Figure 32c shows the vibration vector diagram at the torsion degree of freedom in X direction ( $\theta_x$ ) of each sub-structure point. It can be seen that the vibration amplitude of the planet gear and the carrier is the most obvious at the torsion degree of freedom in X direction ( $\theta_x$ ). Therefore, the vibration mode of the sixth-order mode is the bending vibration of the planet and carrier in the X direction. The main reason is that the carrier is supported by a single-sided bearing, which presents a swinging form of a simply supported beam, thereby resulting in greater vibration.

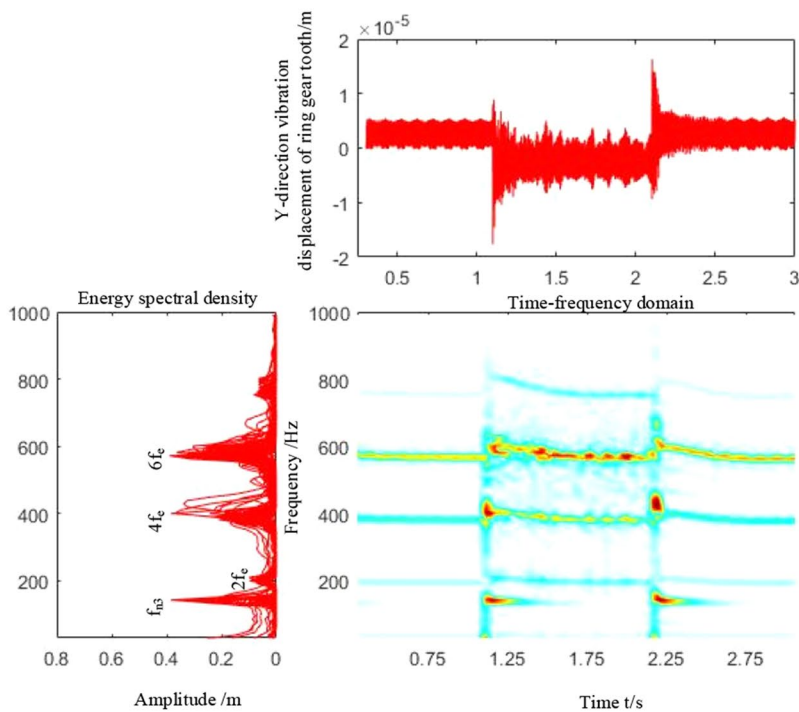
In summary, when the system is coupled, the transient impact phenomenon of the system is effectively reduced, but the influence of the electromagnetic excitation frequency of the SRM is more significant on the dynamic characteristics of the gear system. Meanwhile, at different positions of the system, the free-vibration modes excited by the impact load are different. Therefore, the structural optimization design methods at different positions are different.



**Fig. 29** Short-time Fourier analysis of ring gear tooth radial vibration displacement under impact load with (a) and without coupling (b)

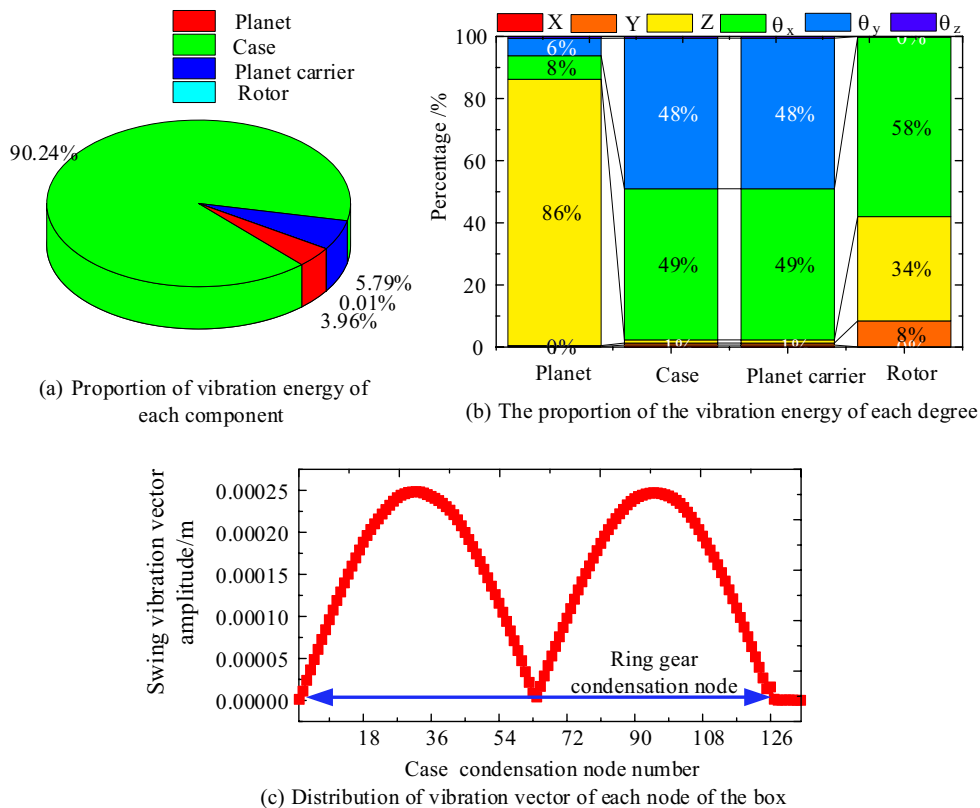


(a) Time-frequency diagram of radial vibration displacement of ring gear teeth(w/o coupling)



(b) Time-frequency diagram of radial vibration displacement of ring gear teeth(w/ coupling)

**Fig. 30** Third-order vibration mode and main vibration components



### Conclusion

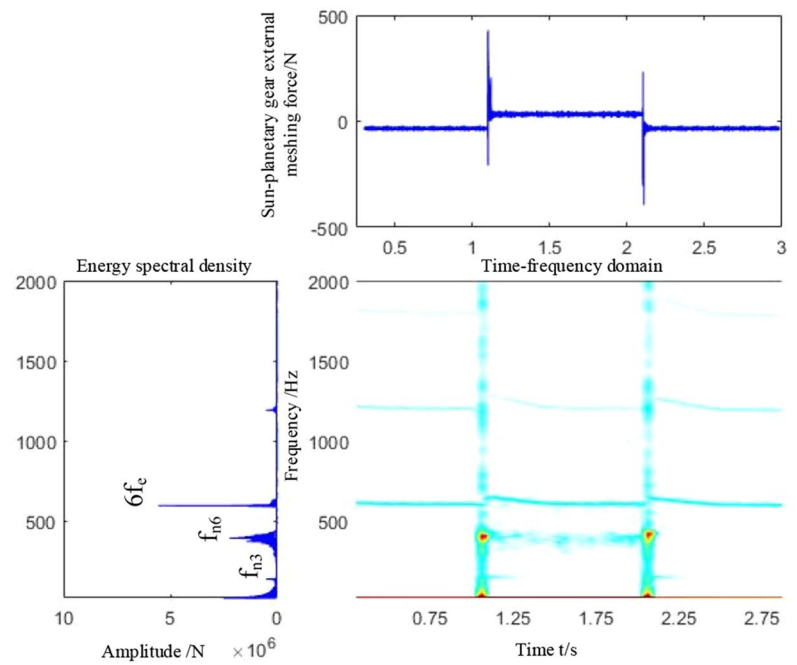
This paper mainly discusses the electromechanical coupling dynamic characteristics of a new type electric drive system structure. The rigid-flexible-electromechanical coupling dynamics model of SRM-PGT system is constructed, which takes into account the flexibility of gear system, and nonlinear electromagnetic characteristics of switched-reluctance motor. The interaction between the mechanical system and the motor system under steady state and transient impact loads is discussed, and the following conclusions are obtained:

1. The dynamic meshing force, bearing force, and gearbox vibration were mainly affected by the electromagnetic excitation of the SRM. The vibration characteristics of the SRM are also affected by the internal excitation of the gear system. Therefore, SRM-PGT is a typical electromechanical strong coupling system. The main excitation frequency of the system originates from the elec-

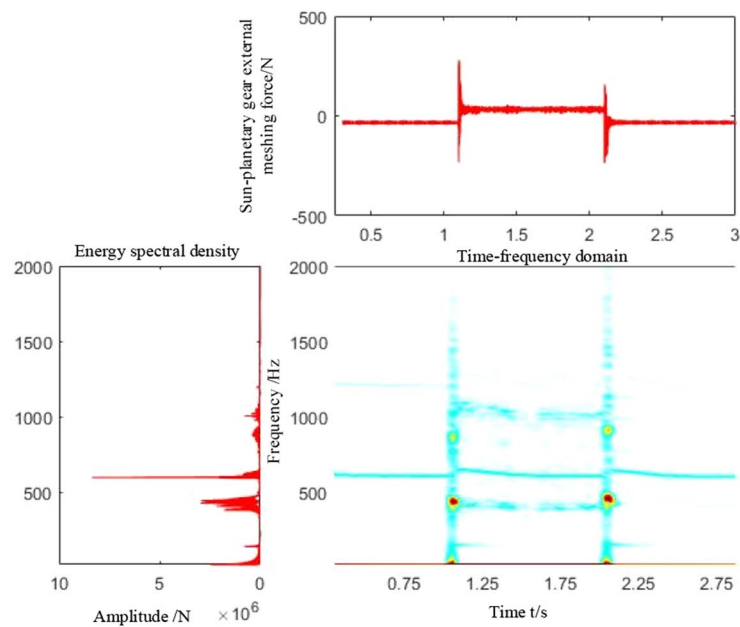
tromagnetic excitation force of the SRM. Meanwhile, reducing the electromagnetic radial force fluctuation can help to reduce the vibration of the SRM-PGT system.

2. In steady-state operation, the presence or absence of coupling has little influence on the dynamic characteristics of the gear. However, when there is coupling, the interaction effect between the motor system and planetary gear system is increased.
3. In the transient process, the coupling plays a key role in reducing the transient impact of the gear system, but it enhances the influence of the electromagnetic excitation frequency on the gear system. Meanwhile, using the modal energy method and mode vector distribution diagram can effectively identify potentially dangerous components. At different positions of the system, the free-vibration modes excited by the impact load are different. Therefore, the selection of measurement points also seriously affects the judgment of potentially dangerous components.

**Fig. 31** Time–frequency map of the sun-planet gear meshing force with and without coupling



(a) Time-frequency analysis diagram of external meshing force of sun- planetary gear(w/o coupling)



(b) Time-frequency analysis diagram of external meshing force of sun- planetary gear(w/ coupling)

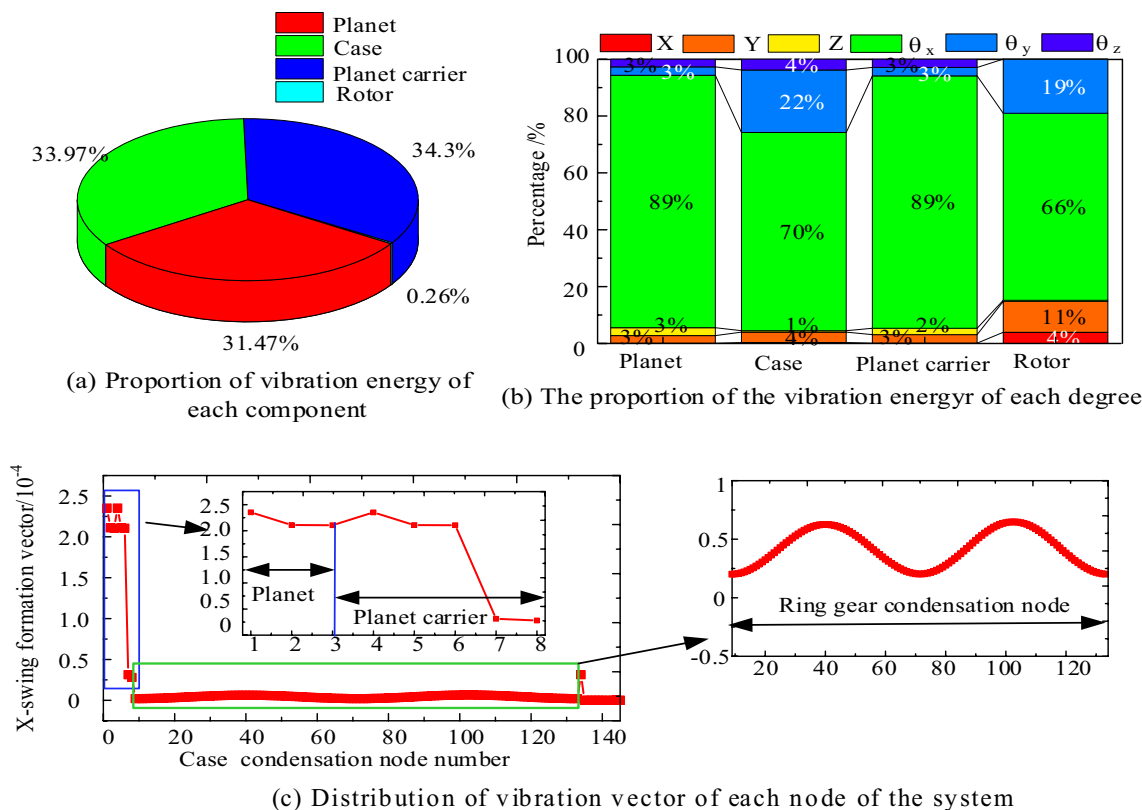


Fig. 32 Sixth-order vibration mode and main vibration components

**Acknowledgements** This work was supported by National key research and development plan (Grant No. 2020YFB2008102), Chongqing Technology Innovation and Application Development Project (Grant No. cstc2019jscx-zdztzxX0047), and China Scholarship Council.

**Author contributions** RC conceptualization, methodology, software, formal analysis, and writing—original draft; CL conceptualization, funding acquisition, resources, and supervision; DQ conceptualization, resources, writing—review and editing, and conceptualization; XD resources, writing—review and editing, conceptualization, resources, and writing—review and editing.

**Declarations**

**Conflict of interest** The authors declare that they have no known competing financial interests or personal relationships that could have appeared to influence the work reported in this paper.

**References**

1. Krishnan R (2017) Switched reluctance motor drives: modeling, simulation, analysis, design, and applications. CRC Press, Boca Raton
2. Miller T (1992) Switched reluctance motors and control
3. Yan Y, Zhiqian D, Qianying Z, Xiaolin W (2010) Stator vibration analysis of bearingless switched reluctance motors, pp 1993–1996

4. Yang Y, Deng Z, Cao X, Yang G, Wang X (2009) Magnetic radial force model of bearingless switched reluctance motors. *Electr Mach Control* 13:377-382+388
5. Husain I, Radun A, Nairus J (2000) Unbalanced force calculation in switched-reluctance machines. *IEEE Trans Magn* 36:330–338
6. Kahraman A (1994) Natural modes of planetary gear trains. *J Sound Vib* 173:125–130
7. Tao S, Yunwen S, Zhimin S et al (2002) Nonlinear dynamics model and equation of planetary gear transmission. *Chin J Mech Eng* 48(003):6–10
8. Tongqiang Y, Yimin S, Ce Z et al (2005) Analysis of free vibration characteristics of helical planetary gear system. *J Mech Eng* 07:50–55
9. Zhou L, Wu S, Li J et al (2016) Establishment of translational torsion model and analysis of nonlinear dynamic characteristics of 2K-H planetary gear train. *J Vib Shock* 35(12):71–76
10. Qiu X, Han Q, Chu F et al (2017) Investigation of parametric instability of the planetary gear under speed fluctuations. *Shock Vibr.* <https://doi.org/10.1155/2017/6851903>
11. Khoozani MK, Poursina M, Anaraki AP (2017) Study of gyroscopic effects on the dynamics and vibrations of double-helical planetary gear set. *Proc Inst Mech Eng Part K J Multibody Dyn* 232(2):199–223
12. Sun Shouqun Xu, Wei ZY et al (2009) Multi-flexible body dynamics analysis of planetary gear inner gear ring. *J Mach Des* 26(11):51–54
13. Chen P (2014) Research on fault mechanism of marine planetary gear tooth broken. Shanghai Jiao Tong University
14. Chen Z, Shao Y, Su D (2013) Dynamic simulation of planetary gear set with flexiblespur ring gear. *J Sound Vib* 332(26):7191–7204

15. Wu X, Parker RG (2008) Modal properties of planetary gears with an elastic continuum ring gear. *J Appl Mech* 75:031014
16. Fan Z, Zhu C, Song C (2019) Dynamic analysis of planetary gear transmission system considering the flexibility of internal ring gear. *Iran J Sci Technol Trans Mech Eng* 44(3):695–706
17. Tatar A, Schwingshackl CW, Friswell MI (2019) Dynamic behaviour of three-dimensional planetary geared rotor systems. *Mech Mach Theory* 134:39–56
18. Wei J, Zhang A, Qin D, Lim TC, Shu R, Lin X, Meng F (2017) A coupling dynamics analysis method for a multistage planetary gear system. *Mech Mach Theory* 110:27–49
19. Wang C, Parker RG (2020) Dynamic modeling and mesh phasing-based spectral analysis of quasi-static deformations of spinning planetary gears with a deformable ring. *Mech Syst Signal Process* 136:106497
20. Liu C, Yin X, Liao Y, Yi Y, Qin D (2020) Hybrid dynamic modeling and analysis of the electric vehicle planetary gear system. *Mech Mach Theory* 150:103860
21. Liu C, Qin D, Liao Y (2017) Electromechanical dynamic analysis for the cutting transmission system of the unmanned long-wall shearer under variable speed process. *J Vibroeng* 19:3191–3206
22. Liu C, Qin D, Liao Y (2015) Electromechanical dynamic analysis for the drum driving system of the long-wall shearer. *Adv Mech Eng* 7:1–14
23. Bai W, Qin D, Wang Y, Lim TC (2018) Dynamic characteristic of electromechanical coupling effects in motor-gear system. *J Sound Vib* 423:50–64
24. Yi Y, Qin D, Liu C (2018) Investigation of electromechanical coupling vibration characteristics of an electric drive multistage gear system. *Mech Mach Theory* 121:446–459
25. Yi Y, Tan X, Xuan L, Liu C (2020) Dynamic interaction behavior of an electric motor drive multistage gear set. *IEEE Access* 8:66951–66960
26. Ho SL, Li HL, Fu WN, Wong HC (2000) A novel approach to circuit-field-torque coupled time stepping finite element modeling of electric machines. *IEEE Trans Magn* 36(36):1886–1889
27. Takemoto M, Suzuki H, Chiba A, Fukao T, Rahman MA (2001) Improved analysis of a bearingless switched reluctance motor. *IEEE Trans Ind Appl* 37(37):26–34
28. Takemoto M, Shimada K, Chiba A, Fukao T (1998) A design and characteristics of switched reluctance type bearingless motors, No. NASA/CP-1998-207654, pp 49–63
29. Husain I, Radun A, Nairus J (2000) Unbalanced force calculation in switched-reluctance machines. *IEEE Trans Magn* 36(36):330–338

**Publisher's Note** Springer Nature remains neutral with regard to jurisdictional claims in published maps and institutional affiliations.